Computational Analysis of Piezoelectric Systems Using A Coupled Multiphysics Finite Element Model

by

Zhiren Zhu

A thesis submitted to The Johns Hopkins University in conformity with the requirements for the degree of Master of Science.

Baltimore, Maryland

August, 2017

Abstract

A multiphysics finite element model framework for coupling transient electromagnetic and dynamic mechanical fields is utilized to perform computational analysis of piezoelectric material systems. The model framework achieves coupling between the mechanical and electromagnetic fields by solving the corresponding governing equations in the time domain, and is capable of predicting the evolution of electric field variables in a conducting medium undergoing dynamic finite deformation. The computational model is then calibrated to reproduce experimentally-characterized behavior of viscoelastic piezo-nanocomposite (p-NC) structures subjected to dynamic loading. The numerical model shows good agreement with experimental results on the loading-frequency dependent piezoelectric output of p-NC systems. Sensitivity study is conducted with the calibrated model to examine the effect of the mechanical input parameters on piezoelectric output of p-NC. Based on the findings, the energy harvesting and sensing performance of p-NC systems can be enhanced by effectively harnessing the viscoelastic properties of the material.

Primary Reader: Professor Somnath Ghosh

Secondary Reader: Professor Sung Hoon Kang

Acknowledgments

I express my gratitude to my adviser, Professor Somnath Ghosh, for sharing his wisdom with me during my time here at Johns Hopkins. I sincerely admire his spirit as a passionate scientist and determination to pursue perfection. It is with great pride to claim that I learned my finite element method from Professor Ghosh.

Thanks also to Professor Sung Hoon Kang for introducing me to the world of functional materials and the insightful discussions that gave meaning to my work. I would also like to acknowledge the help from Jing Li during our collaborative project.

Special thanks go to Shu Guo, for kindly and patiently mentoring me, and helping me tackle countless challenges through the course of my research. I also express my thanks to the other fellow members of the Computational Mechanics Research Laboratory and friends in the Department of Civil Engineering for their continued support.

The work is supported by the Multifunctional Materials & Microsystems division of AFOSR under award ID 2770925044895D. The sponsorship is greatly appreciated. I want to also thank the staffs at Homewood High-Performance Cluster and Maryland Advanced Research Computing Center for supporting my work with the super-computers.

Contents

CONTENTS

List of Tables

List of Figures

Chapter 1

Introduction

Novel materials have recently been introduced to construct multifunctional structures governed by multiphysics principles such as the coupling of mechanical and electromagnetic relations. The multifunctional structures are of great interest for application in consumer electronics, structural health monitors, and aerospace structures.These structures may be active skins of aircraft [1, 2], vibration control devices [3, 4], meta-materials for optical and communication systems [5, 6], as well as high-mobility and stretchable electronics [7–10]. With the increased demand for the design of multifunctional structures governed by multiphysics principles, there is a need for robust computational code frameworks to model the coupled multiphysics problems.

Modeling framework for the evolution of electromagnetic fields in a moving deformable media has been under development for many decades, but the construction of a comprehensively effective framework is still considered to be a challenging task. Finite element analysis of electromagnetic field for signal transmission in antennas has been traditionally carried out in the frequency domain [11]. Yet, solution process in the frequency domain is not suitable when the electromagnetic problem is coupled

Software	Capability	Limitations
ABAQUS	Piezoelectric material analysis with small deformation, low frequency transient EM field	Does not couple high frequency EM fields with ME fields. Lack of piezoelectric material simulation in finite deformation
COMSOL	Coupled low frequency EM field, radio frequency EM field using vector potentials with ME field	Does not fully couple transient EM and ME fields in time domain
ANSYS	Couples EM (HFSS) and structural problems with updated configuration	Does not have two way coupling for EM-ME problems

Table 1.1: Comparison of selected commercial codes for multi-physics simulations

with finite deformation analysis. Furthermore, for multifunctionality, electromagnetic equations are required to be solved in the reference configuration, which necessitates a strong coupling with the deformation field.

Demkowicz and co-workers have developed novel descriptions of hp-adaptive finite element (FE) methods and generalization of the adaptive method for coupled multiphysics problems [12–14]. Electromagnetic forming processes have been simulated with coupled mechanical and electromagnetic fields by Triantafyllidis and co-workers [15, 16]. Finite deformation analysis of piezoelectric composite materials, used in sensors and actuators, have been conducted, but the proposed frameworks were established mostly under quasi-static assumptions [17, 18]. Commercial codes have recently included coupled mechanical-electromagnetic analysis capabilities, but still display certain limitations, as reviewed in [19] and shown here in Table 1.1.

In the present thesis, a generalized framework to couple transient electromagnetic and dynamic mechanical fields is applied to analyze the piezoelectric behaviors of

multifunctional structures. The framework is as introduced in [19, 20, 21], and suits the need to predict the evolution of electrical and magnetic fields and their fluxes in a vibrating substrate undergoing finite deformation. To achieve coupling between fields with disparate frequency ranges, the governing equations are solved in the time domain, as opposed to the frequency domain. A Lagrangian description is invoked, in general accordance with the methods developed in [22, 23, 24]. The coupling scheme maps Maxwell's equations from spatial to material coordinates in the reference configuration. By applying the Euler-Lagrange stationary conditions, weak forms of the coupled dynamic mechanical and transient electromagnetic equations are generated in the reference configuration. From the weak form, the FE equations is developed using the Galerkin's method. Physical variables in the Maxwell's equations are written in terms of a scalar potential and vector potentials, allowing for a more efficient solution process with a reduced number of Maxwell's equations and associated field variables. Introduction of a gauge condition in the FE formulations helps overcome the non-uniqueness of solutions in the reduced set of equations. Additionally, the boundary conditions are appropriately represented in terms of the potentials, rather than the original physical variables. Piezoelectric constitutive relations is implemented in the framework for numerical analysis of piezoelectric materials.

Furthermore, the multiphysics FE model is applied to facilitate the characterization and design of viscoelastic piezo-nanocomposite (p-NC) systems for energy harvesting and sensing applications. This class of composite materials enables the use of

piezoelectricity in a broad range of applications, while assuring good conversion efficiency, flexibility in shape formation, and accommodation of large deformation. Since the polymeric matrix of the piezocomposite is viscoelastic, the piezoelectric performance of the material under dynamic loading is also expected to display frequency dependence. Simulations were performed to calibrate the computational model and reproduce the loading-frequency dependence of piezoelectric output measured in experiments. The computational framework is further utilized to study influence of the material model's input mechanical parameters on the piezoelectric performance under dynamic loading conditions.

The present thesis first reviews the formulation of the multiphysics FE framework in Chapter 2. Governing equations for the problem is reviewed in Sections 2.1, 2.2, and 2.3, and the FE implementation is discussed in Section 2.4. Analysis of the viscoelastic p-NC system is introduced in Chapter 3. The thesis is concluded in Chapter 4.

Chapter 2

Finite Element Model for Coupled Electromagnetic and Mechanical Fields in Piezoelectric Materials

In order to evaluate the evolution of transient electromagnetic field variables in a deformable, conducting medium undergoing finite dynamic deformation, the solution process must comprehensively couple the mechanical and electromagnetic fields through their governing equations. Particularly in the case of piezoelectric materials, the electromagnetic field variables depends on the deformed configuration, while the mechanical field variables are also subjected to induced forces by the electromagnetic field. This requires the implementation of a two-way coupling scheme to capture the interaction between the electromagnetic and mechanical fields.

In the present framework, previously published in [19, 20], a staggered coupling scheme is established between the electric and mechanical fields. At each time step, the mechanical field is first solved, and the electric field is then calculated accordingly in the updated configuration, based on the deformation solution. Information of the

electric field is transferred back to the mechanical field in the following time step, to evaluate the reverse piezoelectric response.

In this chapter, the governing equations for the mechanical, electromagnetic, and piezoelectric problems in the reference configurations and their implementation in the FE framework are reviewed.

2.1 Governing equations for the finite deformation dynamic problem

To model the mechanical response of the conducting medium, the FE framework utilizes the governing equations for a hyperelastic material undergoing finite deformation under dynamic loading conditions. The reference configuration $\Omega_0 = \Omega(t_0)$ is expressed in terms of the material coordinates $X_I, I = 1, 2, 3$, while the current configuration $\Omega(t)$ at time t is represented by the spatial coordinates $x_i, i = 1, 2, 3$. Deformation of the body is expressed using a single-valued mapping function $x_i = \varphi_i(X_J, t)$. Correspondingly, the Cartesian components of the displacement vector in the material coordinates are expressed as: $u_i(X_J, t) = \varphi_i(X_J, t) - \delta_{iJ}X_J$.

Among the many available constitutive relations for hyperelastic material, a modified neo-Hookean material model is utilized in this study. To present the modified neo-Hookean model, we first examine the original neo-Hookean material model, for which the strain energy density function Ψ is expressed in terms of the kinematic

variables as:

$$\Psi = \frac{1}{2}\lambda(\ln J)^2 - \mu \ln J + \frac{1}{2}\mu(C_{II} - 3) \tag{2.1}$$

where μ and λ are the Lamé constants, and

$$C_{IJ} = \frac{\partial x_k}{\partial X_I}\frac{\partial x_k}{\partial X_J} \tag{2.2}$$

is the right Cauchy-Green deformation tensor, and C_{II} is its first invariant, i.e. trace. The positive-valued Jacobian J, which indicates volume change during deformation, is defined in terms of the deformation gradient tensor F_{iJ} as:

$$J = \det(F_{iJ}) > 0 \quad \text{where} \quad F_{iJ} = \frac{\partial x_i}{\partial X_J} \tag{2.3}$$

Notice that the right Cauchy-Green deformation tensor can be expressed in terms of the deformation gradient as: $C_{IJ} = F_{kI}F_{kJ}$.

By definition, the stress-strain relation can be derived from the energy density expression, i.e. Equation 2.1, as:

$$S_{IJ} = 2\frac{\partial \Psi}{\partial C_{IJ}} = \lambda \ln J C^{-1}_{IJ} + \mu(\delta_{IJ} - C^{-1}_{IJ}) \tag{2.4}$$

For the modified version neo-Hookean model used in this study, the strain energy density function is decomposed here into a volumetric part $\Psi^{vol}(J)$ and a deviatoric

part $\Psi^{dev}(\bar{C}_{IJ})$ as:

$$\Psi(J,\bar{C}_{IJ}) = \Psi^{vol}(J) + \Psi^{dev}(\bar{C}_{IJ}) = \frac{1}{2}(\lambda + \frac{2}{3}\mu)(\ln J)^2 + \frac{1}{2}\mu(\bar{C}_{II} - 3) \tag{2.5}$$

Here, $\bar{C}_{IJ} = \bar{F}_{kI}\bar{F}_{kJ}$ represents the volume preserving portion of the deformation, with $\bar{F}_{kI} = J^{-2/3}F_{kI}$, such that $\det \bar{F}_{kI} = 1$.

Stress-strain relation can be derived for the volumetric and deviatoric parts, respectively, as:

$$S^{vol}_{IJ} = 2\frac{\partial \Psi^{vol}}{\partial C_{IJ}} = (\lambda + \frac{2}{3}\mu)\ln J C^{-1}_{IJ} \tag{2.6}$$

$$S^{dev}_{IJ} = 2\frac{\partial \Psi^{dev}}{\partial C_{IJ}} = \mu J^{-2/3}(\delta_{IJ} - \frac{1}{3}C^{-1}_{IJ}C_{KK}) \tag{2.7}$$

with a combined form for the overall material model as:

$$S_{IJ} = S^{vol}_{IJ} + S^{dev}_{IJ} = (\lambda + \frac{2}{3}\mu)\ln J C^{-1}_{IJ} + \mu J^{-2/3}(\delta_{IJ} - \frac{1}{3}C^{-1}_{IJ}C_{KK}) \tag{2.8}$$

Addition to hyperelasticity, viscoelastic material constitutive relation is included in order to study the viscoelastic system presented later in Chapter 3. In this case, the second Piola-Kirchhoff stress at a given time step is expressed as:

$$S^{vol}_{IJ} = 2\frac{\partial \Psi^{vol}}{\partial C_{IJ}} - Q_{IJ} \tag{2.9}$$

where Q_{IJ} is the non-equilibrium viscous stress. The evolution of Q_{IJ} is specified by a rate equation describing the viscoelastic material model [25, 26]:

$$\dot{Q}_{IJ} + \frac{1}{\tau} Q_{IJ} = \frac{(1-\gamma)}{\tau} dev \frac{\partial \bar{\Psi}}{\partial \bar{E}_{IJ}} \tag{2.10}$$

where $\tau \in (0, \infty)$ is relaxation time, $\gamma \in [0, 1)$ is a given parameter, $\bar{\Psi}$ is the deviatoric part of the strain energy density Ψ, and $\bar{E}_{IJ}$ is the volume-preserving part of the strain tensor E_{IJ}.

To obtain the formulation for finite deformation in the reference configuration, first consider the equilibrium of a continuum body in the current deformed configuration:

$$\frac{\partial {}^t\sigma_{ij}}{\partial {}^t x_j} + {}^t \rho b_i = {}^t \rho \ddot{u}_i \tag{2.11}$$

where ${}^t\sigma_{ij} = J^{-1} F_{iK} F_{jL} S_{KL}$ is the Cauchy stress in the current configuration, b_i is the body force per unit volume, ${}^t\rho$ is the density of the deformed material. It is worthwhile to note that the density of the undeformed material is written as ${}^0\rho = J {}^t\rho$.

With the principle of virtual work and applying the divergence theorem, we may express the weak form as:

$$\int_{{}^tV}^t \sigma_{ij} \frac{\partial \delta u_i}{\partial {}^t x_j} d^tV + \int_{{}^tV}^t \rho \ddot{u}_i \delta u_i d^tV = \int_{{}^tS}^t \sigma_{ij} \delta u_i^t n_j d^tS + \int_{{}^tV}^t \rho b_i \delta u_i d^tV \tag{2.12}$$

Note that the integration domain is the current configuration. In order to solve the

problem, the formulation is mapped to the reference configuration. Here, we can use relationships from mass conservation:

$$ {}^0\rho = J^t\rho \quad d^tV = Jd^0V \quad s.t. \quad {}^0\rho d^0V = {}^t\rho d^tV \tag{2.13} $$

to rewrite the weak form as:

$$ \int_{{}^0V} {}^t_0P_{iJ} + \int_{{}^0V} {}^0\rho\ddot{u}_i\delta u_i d^0V = \int_{{}^0S} {}^t_0P_{iJ}\delta u_i N_J d^0S + \int_{{}^0V} {}^0\rho b_i\delta u_i d^0V \tag{2.14} $$

where ${}^t_0P_iJ = J^t\sigma_{ik}F^{-1}_{Jk} = \frac{\partial x_i}{\partial X_K}{}^t_0S_{KJ}$ is the first Piola-Kirchhoff stress. This allows for the equilibrium condition at $t = 0$ in the reference configuration to be expressed as:

$$ \frac{\partial^t_0P_{iJ}}{\partial X_J} + {}^0\rho b_i = {}^0\rho\ddot{u}_i \tag{2.15} $$

2.2 Governing equations for the electromagnetic problem

The governing equations for the electromagnetic problem is based on the conventional Maxwell's equations for a conducting medium. These equations are expressed in the

current configurations in terms of the current coordinate $x_i(t)$ as:

$$d_{i,i} = q_e \qquad \text{Gauss' law of electricity} \tag{2.16a}$$

$$b_{i,i} = 0 \qquad \text{Gauss' law of magnetism} \tag{2.16b}$$

$$\varepsilon_{ijk} e_{k,j} = -\frac{\partial b_i}{\partial t} \qquad \text{Faraday's law of magnetism} \tag{2.16c}$$

$$\varepsilon_{ijk} h_{k,j} = \frac{\partial d_i}{\partial t} + j_i^f \qquad \text{Ampere's law} \tag{2.16d}$$

Here d_i is the Cartesian components of the electrical displacement field vector, q_e is free charge density, b_i are the components of the magnetic induction field vector, e_i is electric field vector, h_i is the magnetic field strength vector, and j_i^f is the free charge current defined as:

$$j_i^f \triangleq j_i^c + q_e \dot{x}_i \tag{2.17}$$

where j_i^c is conducting current and ε_{ijk} is the Levi-Civita permutation symbol. In the absence of magnetization and polarization, the constitutive laws for an isotropic material in the current configuration are given as:

$$d_i = \varepsilon e_i \tag{2.18a}$$

$$h_i = \frac{1}{\mu} b_i \tag{2.18b}$$

$$j_i^c = \sigma(e_i + \varepsilon_{ijk} \dot{x}_j b_k) \tag{2.18c}$$

where permittivity ε, permeability μ, and conductivity σ are material constants.

In order to achieve coupling with the set of mechanical field equations, the Maxwell's equations must be represented in the reference configuration Ω_0. Following the derivation presented in [19, 21], we may arrive at the following form:

$$D_{I,I} = Q_e \tag{2.19a}$$

$$B_{J,J} = 0 \tag{2.19b}$$

$$\varepsilon_{IJK}\frac{\partial}{\partial X_J}E_K = -\frac{d}{dt}B_I \tag{2.19c}$$

$$\varepsilon_{IJK}\frac{\partial}{\partial X_J}H_K = \frac{d}{dt}D_I + J_I^c \tag{2.19d}$$

Note that the electric and magnetic induction fields in the reference configuration is defined as:

$$E_I \triangleq [e_j - \varepsilon_{jmn}(b_m\dot{x}_n)]x_{j,I} \tag{2.20a}$$

$$B_J \triangleq JX_{J,i}b_i \tag{2.20b}$$

and the constitutive laws in the reference configuration are expressed as:

$$D_I = \varepsilon J X_{I,j}\, X_{J,j}\, [E_J + \varepsilon_{JKL}(\frac{\partial X_K}{\partial t} B_L)] = \varepsilon J C^{-1}_{IJ}[E_J + \varepsilon_{JKL}(\frac{\partial X_K}{\partial t} B_L)] \quad (2.21a)$$

$$\begin{aligned} H_J &= h_i x_{i,J} + \varepsilon_{JKL} \frac{\partial X_K}{\partial t} D_L \\ &= \frac{1}{\mu} J^{-1} x_{i,M}\, x_{i,J}\, B_M + \varepsilon_{JKL} \frac{\partial X_K}{\partial t} \left\{ \varepsilon J C^{-1}_{LN}[E_N + \varepsilon_{NPQ}(\frac{\partial X_P}{\partial t} B_Q)] \right\} \\ &= \frac{1}{\mu} J^{-1} C_{MJ} B_M + \varepsilon_{JKL} \frac{\partial X_K}{\partial t} \left\{ \varepsilon J C^{-1}_{LN}[E_N + \varepsilon_{NPQ}(\frac{\partial X_P}{\partial t} B_Q)] \right\} \end{aligned} \quad (2.21b)$$

$$J^c_I = \sigma J C^{-1}_{IJ} E_J \quad (2.21c)$$

Instead of directly solving the variables in the Maxwell's equations, the present framework proposes a scalar potential φ for the electric field and a vector potential $\mathbf{a}$ for the magnetic field, in the current configuration, as primary variables. This approach was followed by Nelson in [27], and effectively reduces the Maxwell's equations from four to two independent equations.

Given that the divergence of the magnetic induction vector $\mathbf{b}$ is zero, the magnetic vector potential $\mathbf{a}$ is derived using a vector identity:

$$\nabla \cdot \mathbf{b} = \nabla \cdot (\nabla \times \mathbf{a}) = 0 \quad \Longrightarrow \quad b_i = \varepsilon_{ijk} a_{k,j} \quad (2.22)$$

This allows for the Faraday's law in the current configuration, i.e. Equation 2.16c, to be expressed as:

$$\varepsilon_{ijk}(e_k + \dot{a}_k)_{,j} = 0 \quad (2.23)$$

Since the curl of gradient of any scalar field is a null vector, the gradient of ε is placed in the LHS to yield the form:

$$\varepsilon_{ijk}(e_k + \dot{a}_k + \varepsilon_{,k})_{,j} = 0 \tag{2.24}$$

allowing for the expression of electric field using the mixed potentials:

$$e_k = -\varphi_{,k} - \dot{a}_k \tag{2.25}$$

Introduction of the potentials in the Gauss' law of magnetism of Equation 2.16b results in identity. The remaining Maxwell's equations are reformulated as:

$$\nabla^2\varphi + \frac{\partial}{\partial t}(a_{i,i}) = -q_e \tag{2.26a}$$

$$(\nabla^2 a_i - \mu\varepsilon\frac{\partial^2 a_i}{\partial t^2}) - (a_{k,k} + \mu\epsilon\frac{\partial\varphi}{\partial t})_{,i} = -\mu j_i \tag{2.26b}$$

To obtain a corresponding reduced form of the Maxwell's equations in the reference configuration, the potentials is defined with the transformation functions as:

$$\Phi = \varphi - \frac{dx_i}{dt}a_i \tag{2.27a}$$

$$A_K = a_i x_{i,K} \tag{2.27b}$$

In the reference configuration, the electric and magnetic induction fields can be

written in terms of the mixed potentials as:

$$E_I = -\Phi_{,J} - \frac{\partial A_I}{\partial t} \tag{2.28a}$$

$$B_I = \varepsilon_{IJK} A_{K,J} \tag{2.28b}$$

which can be substituted to the Maxwell's Equations 2.19a and 2.19d to generate the governing equations:

$$\left(\varepsilon J C^{-1}_{IJ} \tilde{E}_J\right)_{,I} = Q_e \tag{2.29a}$$

$$\varepsilon_{IJK}\left(\frac{1}{\mu J} C_{KL}\varepsilon_{LMN} A_{N,M} + \varepsilon_{KPQ}\frac{\partial X_P}{\partial t}\varepsilon J C^{-1}_{QR}\tilde{E}_R\right)_{,J} = \frac{d}{dt}\varepsilon J C^{-1}_{IP}\tilde{E}_P + \sigma J C^{-1}_{IQ}\left(-\Phi_{,Q} - \dot{A}_Q\right) \tag{2.29b}$$

where $\tilde{E}_I$ is defined as:

$$\tilde{E}_I = E_I + \varepsilon_{IJK}\frac{\partial X_J}{\partial t}B_K = -\Phi_{,I} - \dot{A}_I + \varepsilon_{IJK}\frac{\partial X_J}{\partial t}\varepsilon_{KMN}A_{N,M} \tag{2.30}$$

Although the reduced representation of Maxwell's equations is advantageous computationally, it also leads to non-uniqueness of solution for certain state of the EM fields. Therefore, the Coulomb gauge condition is enforced, as proposed in [18, 28, 29], to avert the non-uniqueness. This condition is states as:

$$A_{I,I} = 0 \tag{2.31}$$

which implies a restriction to the irrotational term in Equation 2.28b.

The weak form of the transient electromagnetic problem is derived using the Hamilton's principle [22, 27]. By minimizing the action functional S over the time range t_1 to t_2, which is defined in terms of the time-dependent Lagrangian density $\mathcal{L}$ in the reference domain:

$$\delta S = \delta \int_{t_1}^{t_2} \int_{\Omega_0} \mathcal{L} d\Omega_0 dt = 0 \tag{2.32}$$

where the Lagrangian density in the reference and current configuration, $\mathcal{L}$ and l respectively, are given as:

$$\mathcal{L} = Jl = (\frac{\epsilon}{2} e_i e_i - \frac{1}{2\mu} b_j b_j + j_k a_k - q\varphi) \tag{2.33}$$

and can be expressed in terms of the scalar and vector potentials in the reference configuration as:

$$\mathcal{L} = \frac{\varepsilon J}{2} C_{JK}^{-1} \tilde{E}_J \tilde{E}_K - \frac{J^{-1}}{2\mu} (C_{LM} B_L B_M) + J_N A_N - Q\Phi \tag{2.34}$$

Furthermore, the gauge condition is implemented using a penalty method to constrain the vector potential, following [28, 18, 29]. This adds an additional term $\frac{1}{p}(\nabla \cdot \mathbf{A})^2$ to the Lagrangian density function:

$$\mathcal{L} = \frac{\varepsilon J}{2} C_{JK}^{-1} \tilde{E}_J \tilde{E}_K - \frac{J^{-1}}{2\mu} (C_{LM} B_L B_M) + J_N A_N - Q\Phi + \frac{1}{p} (A_{P,P})^2 \tag{2.35}$$

The penalty coefficient $1/p$ is usually of the order of the electric permittivity ε.

Setting the variation of S with respect to Φ and $\mathbf{A}$ to be zero, we obtain:

$$S_{,\Phi}[\delta\Phi] = \int_{t_1}^{t_2} \int_{\Omega_0} \mathcal{L}_{,\Phi}[\delta\Phi]\Omega_0 dt = 0 \tag{2.36a}$$

$$S_{,\Phi}[\delta\mathbf{A}] = \int_{t_1}^{t_2} \int_{\Omega_0} \mathcal{L}_{,\mathbf{A}}[\delta\mathbf{A}]\Omega_0 dt = 0 \tag{2.36b}$$

Given arbitrary t_1 and t_2, the above leads to:

$$\int_{\Omega_0} \mathcal{L}_{,\Phi}\,[\delta\Phi] dV_0 = \int_{\partial\Omega_0} N_I \left(\varepsilon J C^{-1}_{IJ} \tilde{E}_J \delta\Phi\right) dS_0 - \int_{\Omega_0} \left(\varepsilon J C^{-1}_{IJ} \tilde{E}_J - Q\right) \delta\Phi_{,I}\, dV_0 = 0 \tag{2.37a}$$

$$\begin{aligned}
&\int_{\Omega_0} \mathcal{L}_{,\mathbf{A}}\,[\delta\mathbf{A}] dV_0 = \int_{\partial\Omega_0} N_L(\varepsilon_{KLM} Q_M \delta A_K) dS_0 - \frac{2}{p}\int_{\partial\Omega_0} A_{R,R}\, N_K \delta A_K dS_0 + \\
&\int_{\Omega_0} \varepsilon_{SPR} Q_P \frac{\partial}{\partial X_R} \delta A_S dV_0 - \int_{\Omega_0} \frac{d}{dt} \varepsilon J C^{-1}_{KJ} \tilde{E}_J \delta A_K dV_0 - \int_{\Omega_0} \sigma J C^{-1}_{KI} E_I \delta A_K dV_0 + \\
&\frac{2}{p}\int_{\Omega_0} A_{R,R}\, \delta A_{K,K}\, dV_0 = 0
\end{aligned} \tag{2.37b}$$

with the condensed term expressed as:

$$Q_M = \frac{1}{\mu J} C_{MN} B_N + \varepsilon_{MNP} \frac{\partial X_N}{\partial t} \varepsilon J C^{-1}_{PQ} \tilde{E}_Q \tag{2.38}$$

2.3 Governing equations for the piezoelectric problem

The piezoelectric effect is commonly analyzed and studied under small deformation setting due to its natural properties. Common examples of piezoelectric materials include crystals and ceramics, which can be adequately analyzed with the elastic constitutive equations of small deformation. The electric field is also calculated in the same configuration. A set of constitutive relations is well established for this class of materials [27, 30–32], and will be first reviewed here.

The canonical electro-mechanical power per unit volume of the continuum is,

$$\dot{e} = \sigma_{ij}\dot{\varepsilon}_{ij} + e_k\dot{d}_k \tag{2.39}$$

where e is the internal energy density, σ_{ij} is the Cauchy stress, $\varepsilon_{ij} = (u_{i,j} + u_{j,i})/2$ is the infinitesimal strain tensor from displacement u_i, d_k is the electric displacement field, and $e_k = \phi_{,k}$ is the electric field derived from electric potential.

Following the formulation by Nelson in [27], define electric enthalpy density h for small deformation:

$$h = e - e_i d_i \tag{2.40}$$

which can be combined with Equation 2.39 to obtain:

$$\dot{h} = \sigma_{ij}\dot{\varepsilon}_{ij} - d_i\dot{e}_i \tag{2.41}$$

Noticing the implication that h is a function of strain ε_{ij} and electric field e_k, propose the functional form:

$$h = \frac{1}{2}C^E_{ijkl}\varepsilon_{kl}\varepsilon_{ij} - \frac{1}{2}\epsilon^S_{ij}e_je_i - e_{imn}\varepsilon_{mn}e_i \tag{2.42}$$

which yields the expressions for Cauchy stress σ_{ij} and electric displacement d_i:

$$\sigma_{ij} = \frac{\partial h}{\partial \varepsilon_{ij}} = C^E_{ijkl}\varepsilon_{kl} - e_{kij}e_k \tag{2.43}$$

$$d_i = \frac{\partial h}{\partial e_i} = e_{imn}\varepsilon_{mn} = \epsilon^S_{ij}e_j \tag{2.44}$$

Then, from Equations 2.40 and 2.42, we express the stored energy as:

$$e = \frac{1}{2}C^E_{ijkl}\varepsilon_{kl}\varepsilon_{ij} + \frac{1}{2}\epsilon^S_{ij}e_je_i \tag{2.45}$$

Although this set of constitutive equations is not the only form developed for piezoelectric materials, as shown by Nelson in [27], it is widely employed and therefore selected suitable for our model framework.

In order to study piezoelectricity under finite deformation, it is necessary to de-

velop a Lagrangian description. This can be achieved based on the general form of Maxwell's equations presented in the previous section. For the case of piezoelectric application, free charge Q_e and conducting current J_I^e do not exist in the material, and the magnetic field has negligible effect on the electric field. This allows for the governing equations to be reduced to the following form:

$$D_{I,I} = 0 \tag{2.46a}$$

$$B_{J,J} = 0 \tag{2.46b}$$

$$\varepsilon_{IJK} \frac{\partial}{\partial X_J} E_K = 0 \tag{2.46c}$$

$$\varepsilon_{IJK} \frac{\partial}{\partial X_J} H_K = \frac{d}{dt} D_I \tag{2.46d}$$

By Poynting's theorem, multiple E_I on both sides of Equation 2.46d and subtract the product of Equation 2.46c multiplied by H_I on both sides, then using the identity $-\left(\varepsilon_{IJK} E_J H_K\right)_{,I} = E_I \varepsilon_{IJK} \frac{\partial}{\partial X_J} H_K - H_I \varepsilon_{IJK} \frac{\partial}{\partial X_J} E_K$, the following relation is obtained:

$$-(\varepsilon_{IJK} E_J H_K)_{,I} = E_I \dot{D}_I \tag{2.47}$$

which can be integrated over the reference configuration, and then applied divergence theorem to obtain:

$$\int_{\partial\Omega_0} -\varepsilon_{IJK} E_J H_K N_I dS_0 = \int_{\Omega_0} E_I \dot{D}_I dV_0 \tag{2.48}$$

The LHS of the above equation is the flux of electromagnetic energy leaving the system from the boundary, while the RHS represents the rate of change in the electromagnetic energy of the system. This establishes the energy balance of the system.

Following derivation framework presented by Holzapfel in [33], a strong form of Clausius-Planck inequality for the piezoelectric system can be obtained based on the laws of thermodynamics:

$$D_{int} = E_I \dot{D}_I + S_{IJ} \dot{E}_{IJ} - \dot{e} + \Theta \dot{\eta} \geq 0 \tag{2.49}$$

where D_{int} is the internal dissipation of the system, Θ is absolute temperature, and η is entropy per unit volume. Detail of the derivation process can be found in [21].

By defining Helmholtz free energy as:

$$\Psi = e - \Theta \eta \tag{2.50}$$

Equation 2.49 can be rewritten as:

$$D_{int} = E_I \dot{D}_I + S_{IJ} \dot{E}_{IJ} - \dot{\Psi} + \eta \dot{\Theta} \geq 0 \tag{2.51}$$

When there is no internal dissipation, i.e. $D_{int} = 0$, and thermal effect is ignored, the following equality holds:

$$E_I \dot{D}_I + S_{IJ} \dot{E}_{IJ} - \dot{\Psi} = 0 \tag{2.52}$$

Furthermore, using Legendre transformation, define electric enthalpy density in the reference configuration as:

$$\mathcal{H} = \Psi - E_I D_I \tag{2.53}$$

Taking time derivative of the electric enthalpy density, the following relation is obtained upon manipulations:

$$\dot{\mathcal{H}} = S_{JK}\dot{E}_{JK} - \dot{E}_I D_I \tag{2.54}$$

which gives the generalized constitutive relationship for piezoelectric material:

$$S_{IJ} = \frac{\partial \mathcal{H}}{\partial E_{IJ}} \tag{2.55}$$

$$D_K = \frac{\partial \mathcal{H}}{\partial E_K} \tag{2.56}$$

In the piezoelectric system, the coupling between mechanical and electric fields is achieved by a piezoelectric constant $\mathfrak{E}_{KIJ}$. Following the form of electric enthalpy density in the current configuration, as presented in Equation 2.42, a form for the electric enthalpy density in the reference configuration is proposed as:

$$\mathcal{H} = \Psi^{ME}(C_{IJ}) - \mathfrak{E}_{KIJ}E_{IJ}E_K - \frac{1}{2}\varepsilon J C^{-1}_{IJ} E_I E_J \tag{2.57}$$

where $\Psi^{ME}(C_{IJ})$ is the stored energy density for the hyperelastic material model. Substituting this proposed form into Equations 2.55 and 2.56, respectively, the full expression for the second Piola-Kirchhoff stress S_{IJ} and electric displacement D_K is obtained:

$$S_{IJ} = \frac{\partial \mathcal{H}}{\partial E_{IJ}} = \underbrace{\frac{\partial \Psi^{ME}}{\partial E_{IJ}}}_{S_{IJ}^{ME}} - \underbrace{\mathfrak{E}_{KIJ} E_K}_{S_{IJ}^{Piezo}} - \underbrace{\frac{1}{2}\varepsilon J \left[\left(E_P C_{PQ}^{-1} E_Q \right) C_{IJ}^{-1} - E_p E_Q \left(C_{PI}^{-1} C_{JQ}^{-1} + C_{PJ}^{-1} C_{IQ}^{-1} \right) \right]}_{S_{IJ}^{Maxwell}} \tag{2.58}$$

$$D_K = -\frac{\partial \mathcal{H}}{\partial E_K} = \mathfrak{E}_{KIJ} E_{IJ} + \varepsilon J C_{LK}^{-1} E_L \tag{2.59}$$

2.4 Finite element implementation of the coupled problem

For the coupled mechanical-electromagnetic problem, numerical implementation of the weak forms is conducted with a staggered approach, where the dynamic displacement field is solved first, followed by the electromagnetic problem. The semi-discretization method involving separation of variables is used to represent the variables as discrete functions of space, while being continuous functions of time.

In the case of 8-noded brick elements, as implemented in the present framework, independent variables, viz. displacements, scalar potential, and vector potential,

within each element e are interpolated as:

$$\mathbf{u}^e(\mathbf{X},t) \approx \sum_{\alpha=1}^{8} \mathbf{u}_\alpha^e(t) N_\alpha^e(\mathbf{X}) \tag{2.60a}$$

$$\Phi^e(\mathbf{X},t) \approx \sum_{\alpha=1}^{8} \Phi_\alpha^e(t) N_\alpha^e(\mathbf{X}) \tag{2.60b}$$

$$\mathbf{A}^e(\mathbf{X},t) \approx \sum_{\alpha=1}^{8} \mathbf{A}_\alpha^e(t) N_\alpha^e(\mathbf{X}) \tag{2.60c}$$

where $\mathbf{N}(\mathbf{X})$ are the trilinear isoparametric shape functions of the brick element [34]. It must be noted that the same finite element mesh is used for the solutions of mechanical and electromagnetic field variables. The implicit time integration Newmark-beta method, which assumes constant average acceleration in each time step [35, 36], is implemented here for time integration in the dynamic mechanical problem. For the electromagnetic field, a backward Euler method is implemented [19, 37].

For efficient computation of the large degrees of freedom (DOF) problems, the finite element code is parallelized using available libraries. The ParMETIS library [38] is utilized to decompose the computational domain and distribute to multiple processors. Subsequently, parallelization of the code is accomplished by employing the Portable Extensible Toolkit for Scientific Computation (PETSC) library [39], a Message Passing Interface (MPI) based library.

2.5 Conclusion

A finite element framework that couples finite deformation dynamic problems with transient electromagnetic problems is reviewed in this chapter. To examine the effect of material deformation on the electromagnetic field variables, reference configuration formulation of the governing equations is developed, and weak forms for the mechanical and electromagnetic problems are constructed. Additionally, piezoelectric material relation is incorporated for analysis of two-way coupling between the mechanical and electromagnetic fields. With the established framework, evolution of electric field in a piezoelectric material undergoing dynamic finite deformation can be analyzed.

Chapter 3

Analysis of Viscoelastic Piezo-nanocomposite System

Polymer-based piezoelectric nanocomposite (p-NC), made of polymeric matrix and piezoelectric particles with conductive additives, is a class of materials that enables the use of piezoelectricity in a broad range of applications. Since the polymeric matrix is viscoelastic, it is expected that the piezoelectric performance of the material under dynamic loading displays frequency dependence. In this chapter, an analytical model describing piezoelectric behavior of viscoelastic systems is presented, and simulations were performed with the multiphysics FE model to predict the evolution of electric field in the p-NC systems undergoing finite deformation.

3.1 Motivation

There has been a continuously growing interest in the use of nanogenerators for sustainable and portable power applications through harvesting of mechanical energy. Active research has been conducted to utilize devices made of piezoelectric materials as power sources for wearable electronics [40, 41], healthcare devices [42, 43],

and self-powered sensors [44, 45], by harvesting energy from ambient vibration and physical activities. The earliest form of nanogenerators were based on piezoelectric ZnO nanowires [40, 46–48]. Perovskite-structured ceramics, such as lead zirconate titanate (PZT) and barium titanate (BTO) have been later used for their high conversion efficiency [49–51]. However, these ceramic materials are brittle and allow for very limited amount of deformation prior to failure. Piezoelectric polymers, such as polyvinylidene fluoride (PVDF), have also been used for energy harvesting. Despite good piezoelectric properties and mechanical stabilities, the polymeric materials have limitations in shape formation and allowable strains [41, 52, 53].

Polymer-based piezoelectric composite (p-NC) is a class of piezoelectric materials that display good conversion efficiency, flexibility in shape formation, and accommodation of large deformation [54–56]. To improve the energy generation capability of piezocomposites, previous studies determined optimal composition of the nanocomposite materials by measuring electric output while varying ratio among the constituents [54, 57, 58]. Studies have also been conducted to examine the effects of particles shapes [59] and polymeric matrix properties [60] on piezoelectric performance. Yet, there is no quantitative understanding to relate the viscoelastic properties of the composite materials with their piezoelectric properties.

In contrast to elastic materials which store all external work when loaded and release the stored energy when unloaded, viscoelastic materials are expected to display energy dissipation during a loading-unloading cycle. As a result of energy dissipation

in viscoelastic material, a reduced amount of mechanical energy is ultimately converted to piezoelectric particles. Therefore, it is critical to harness the viscoelastic properties of the p-NC system to further enhance piezoelectric performance.

3.2 Analytical model for piezoelectricity in viscoelastic systems

An analytical model is proposed to describe the frequency-dependence of piezoelectric performance in a viscoelastic system. Consider a thin plate of p-NC subjected to uniaxial compression. During the deformation process of the viscoelastic p-NC, part of the total work is dissipated as heat through viscous loss, while the remaining energy is stored as elastic strain energy. The stored elastic energy is then transferred to electrical energy. The total work input to the piezoelectric particles, W_{piezo}, can thus be written as

$$W_{piezo} = V_{piezo}(U_S - U_D) \tag{3.1}$$

where V_{piezo} is the volume of the piezoelectric particles, while U_S and U_D are the stored and dissipated energy density, respectively. Here, it is assumed that the p-NC is transversely isotropic with a polarization direction normal to the loaded surface. In terms of the output electric field $\mathbf{E}$, the electrical energy density, U_e, may be expressed as

$$U_e = \frac{1}{2}\varepsilon_{piezo}|\mathbf{E}|^2 \tag{3.2}$$

where ε_{piezo} is permittivity of the piezoelectric particle. When electric charges are generated by the piezoelectric particles, the total electric potential energy, W_e, is

$$W_e = VU_e = \frac{1}{2}V\varepsilon_{piezo}|\mathbf{E}|^2 \tag{3.3}$$

where V is the total volume of the p-NC material.

Since the electric potential energy is generated from the mechanical energy applied to the piezoelectric particles, we may assume that the converted electrical energy is equal to the work input, i.e. $W_e = W_{piezo}$. This allows for the magnitude of the output electric field to be written as

$$|\mathbf{E}| = \sqrt{\frac{2V_{piezo}(U_S - U_D)}{V\varepsilon_{piezo}}} \tag{3.4}$$

Piezoelectric coefficient, d_{ij}, is commonly used to quantify the charge generation due to application of stress, and this evaluated by the relation

$$d_{ij} = \frac{\rho_i}{\sigma_j} \tag{3.5}$$

where ρ_i is the charge density corresponding to induced electric field in the i direction and σ_j is applied stress in the j direction, where a Kelvin notation system is employed to express the stress tensor components. For example, in the case where the material is polarized along the "3" direction, d_{33} indicates the charge density along the po-

larization direction, due to applied normal stress in the same direction (σ_3 in Kelvin notation, or σ_{33} in full notation).

It is assumed here that E_3 is the only non-zero component in the induced electric field vector, and therefore, with Gauss' law

$$\rho_3/\varepsilon_c = \nabla \cdot \mathbf{E} = |\mathbf{E}| = E_3 \tag{3.6}$$

where ε_c is the overall permittivity of the composite material. Therefore, the piezoelectric constant of the p-NC can be written as

$$d_{33} = \frac{\rho_3}{\sigma_3} = \frac{\varepsilon_c}{\sigma_3}\sqrt{\frac{2V_{piezo}(U_S - U_D)}{V\varepsilon_{piezo}}} \tag{3.7}$$

Note that in the present study, it is assumed that only the d_{33} component is non-zero for the piezoelectric coefficient. Equation 3.7 suggests that the piezoelectric coefficient is related to the volume fraction of piezoelectric fillers and the permittivity of the p-NC. In addition, energy dissipation during viscoelastic deformation is expected to contribute to the piezoelectric performance, especially when the material is subjected to dynamic loading conditions.

Viscoelastic materials are often modeled mathematically as systems composed of elastic springs and viscous dashpots. In this study, we consider a standard linear solid model [61–64] for the viscoelastic material, where an elastic spring is connected in parallel with a Maxwell unit. A Maxwell unit contains a spring and a dashpot

connected in series. The dynamic behavior of the viscoelastic material is described by a pair of moduli: the storage modulus, $E^{'}$, and loss modulus, $E^{''}$. The moduli $E^{'}$ and $E^{''}$ are used to define the storage and dissipation of energy, respectively, when the viscoelastic material is dynamically loaded.

In the case of a standard linear solid model, at the point of maximum strain, ε_3, in a sinusoidal excitation, the stored energy per unit volume in the system is given by

$$U_S = \frac{1}{2}\varepsilon_3^2 E^{'} \tag{3.8}$$

and the dissipated energy per unit volume during quarter cycle is written as

$$U_D = \frac{1}{4}\pi\varepsilon_3^2 E^{''} \tag{3.9}$$

This allows us to combine Equations 3.7, 3.8, and 3.9 to obtain an expression for the piezoelectric constant under dynamic loading condition:

$$d_{33} = \frac{\varepsilon_c}{\sigma_3}\sqrt{\frac{2V_{piezo}[E^{'}(\varepsilon_3^2/2) - E^{''}(\pi\varepsilon_3^2/4)]}{V\varepsilon_{piezo}}} \tag{3.10}$$

Additionally, the effective modulus of the material can be written as $E = \sqrt{E^{'2} + E^{''2}}$, while satisfying $\varepsilon_3 = \sigma_3/E$. Therefore, Equation 3.10 can be rewritten as

$$d_{33} = \frac{\varepsilon_c}{\sqrt{E^{'2} + E^{''2}}}\sqrt{\frac{2V_{piezo}(E^{'}/2 - \pi E^{''}/4)}{V\varepsilon_{piezo}}} \tag{3.11}$$

This final form shows that the piezoelectric coefficient, d_{33}, in a dynamically loaded viscoelastic p-NC is a function of the volume fraction of piezoelectric fillers, overall permittivity of the p-NC, and the dynamic moduli of the viscoelastic material.

3.3 Calibration of computational model

Experimental studies were conducted on synthesized specimens of piezoelectric nanocomposites. Specimens of different viscoelastic properties were produced based on polydimethylsiloxane (PDMS) matrix, barium titanate nanoparticles (BTO NPs), and multi-walled carbon nanotubes (CNTs) conductive additives. By adjusting the ratio between monomer and cross-linker of the PDMS matrix, mechanical properties of the p-NCs were altered. Here, we study three different specimens, with mixing ratios between PDMS monomer and curing agent to be 5:1, 10:1, and 20:1, by mass, respectively. After curing, Au/Cr electrodes were deposited on top and bottom surfaces of the p-NCs using sputtering deposition.

Under quasi-static loading condition, the average Young's moduli of the 5:1, 10:1, and 20:1 specimens were measured to be 1.32 MPa, 1.72 MPa, and 0.45 MPa, respectively. The elastic moduli showed very small variation between specimens with equal mixing ratio of monomer and curing agent, even though the nanofillers were randomly distributed in the composite material. Poling process was conducted to align dipoles across the thickness direction ("3-direction"), and permittivities of the p-NCs were measured to be 3.04×10^{-11} F/m, 3.26×10^{-11} F/m, and 3.95×10^{-11}

F/m for the 5:1, 10:1, and 20:1 specimens, respectively. Larger portion of PDMS monomer corresponded to higher dielectric constant.

The storage and loss moduli of the prepared p-NCs were measured with dynamic mechanical analyzer (DMA, TA Instruments TA Q800) at a constant strain of 0.5%. As functions of loading frequency, the dynamic moduli of the p-NCs are shown in Figure 3.1. Additionally, the dielectric constant of the p-NC was measured as a function of frequency. It was found that for each of the three types of p-NC specimens tested, the dielectric constant remain constant at the loading frequency range of 1 to 100 Hz studied.

A piezoelectric dynamic measurement setup was constructed to characterize the piezoelectric performance of the p-NCs under dynamic loading conditions. A mini-shaker was used to apply cyclic loading to the p-NCs, while the generated loads were monitored by a load cell (LRM200, 10 lb, Futek). As the p-NC is compressed by the applied loading, piezoelectric potential is generated across its thickness. The generated electrical charges were measured by a combination of charge amplifier (piezo film lab amplifier, TE Connectivity) and an oscilloscope (TDS2024B, Tektronix). At each loading frequency, the peak surface charge density during the cyclic loading was monitored to evaluate the piezoelectric performance, as shown in Figure 3.2b.

Utilizing the multiphysics FE framework, a computational model for the p-NC material is then calibrated to reproduce the dependence of piezoelectric performance on loading frequency, and allow for extensive studies to determine an optimal set of

mechanical parameters for the p-NC.

The uniaxial cyclic compression tests of the 20:1, 10:1 and 5:1 p-NCs were first simulated, in which the steady-state peak output surface charge density values were compared with the experimental measurements. At each loading frequency, the piezoelectric coefficient of the material was determined according to the analytical model of Equation 3.11, while the storage and loss moduli are the DMA-measured values shown in Figure 3.1. In the FE framework, viscoelastic behavior of material is described by a pair of mechanical parameters, instantaneous modulus modulus E_0 and viscous relaxation term μ_0. The parameters are calibrated to satisfy the following two conditions:

$$E_\infty = E_0(1 - \mu_0) \tag{3.12}$$

$$E^{'}(\omega) = E_\infty + E_0\mu_0\frac{(\omega\tau)^2}{1 + (\omega\tau)^2} \tag{3.13}$$

where ω is the angular frequency of the applied loading, E_∞ is the equilibrium long-term elastic modulus determined by the quasi-static loading tests, and $E^{'}(\omega)$ and τ are the storage modulus and relaxation time determined by the dynamic loading tests.

The 3D mesh and boundary conditions of the model are depicted in Figure 3.2a. The plate was grounded at the bottom surface by setting its electric potential to $\phi = 0$, and uniform cyclic compression was applied on the top surface, with traction

magnitude described by

$$T(t) = \frac{T_p}{2}[1 + \sin(\omega t - \frac{\pi}{2})] \tag{3.14}$$

where T_p is the maximum prescribed compression in the cyclic loading process, set to be $T_p = 400$ Pa here, equal to the peak load applied in the dynamic compression experiment.

Difference of electric potential $\Delta\phi$ across the thickness of the plate was monitored, and peak value at steady-state, $\Delta\phi_p(T_p, \omega)$, was recorded to compute the peak surface charge density $\rho_p(T_p, \omega)$ according to the relation

$$\rho_p(T_p, \omega) = \frac{\varepsilon_0 \varepsilon_r}{d} \Delta\phi_p(T_p, \omega) \tag{3.15}$$

where d is the plate thickness, $\varepsilon_0 = 8.85 \times 10^{-12}$ F·m^{-1} is the vacuum permittivity, and ε_r is the relative permittivity of the material. The FE predictions of $\rho_p(T_p, \omega)$ are compared with experiment results in Figure 3.2b. As observed, the FE model with the calibrated material parameters is able to capture the piezoelectric behavior in the p-NCs under uniaxial cyclic compression and reproduce the relation between loading frequency and peak steady-state charge output. In the range of investigated applied loading frequency, the increase of loading frequency corresponded to a decrease of peak piezoelectric output, at a constant value of peak load. This result again confirms that the viscoelasticity of the composite material affects the dynamic piezoelectric performance of p-NC systems.

3.4 Piezoelectric performance of p-NC under dynamic large deformation

Since a major advantage of the p-NC is its accommodation of large deformation, it is of great interest to investigate the piezoelectric performance of the material under dynamic large deformation. Simulations were performed on uniaxial cyclic tension and compression of the 20:1 p-NC material model (quasi-static modulus $E_\infty = 450$ kPa) at a frequency of 10Hz. Here, peak loading values of $T_p = \pm 1$ kPa, ± 10 kPa, and ± 100 kPa were examined, with the loading pattern described by Equation 3.14. The applied loading values in the latter sets are sufficient for large deformation to occur in the material. Additionally, the same set of simulations were performed on a modified material model with Poisson's ratio of $\nu = 0.30$ and other input parameters, viz. E_0, μ_0, τ, d_{33}, and ε_r, assumed to be unchanged. The original material model, calibrated earlier according to the experiment measurement, is nearly-incompressible, with Poissons ratio set as $\nu = 0.499$.

The measured peak magnitude of surface charge density in the aforementioned cases and the time histories of surface charge density are shown in Figure 3.3. It is observed that, given an equal magnitude of peak load $|T_p|$, cyclic tension produces a higher output charge density than is produced by cyclic compression, and the advantage of applying cyclic tension is more profound when $|T_p|$ is high and also when the material is nearly incompressible. For the compressible material model ($\nu = 0.30$),

the electric field generated under cyclic tension and compression are in opposite directions, which can be noticed from the time history of output charge in Figures 3.3b, 3.3c and 3.3d. However, this is not the case for the nearly-incompressible material model ($\nu = 0.499$). When the nearly-incompressible material is subjected to cyclic compression of relatively large peak load, the direction of piezoelectric field is in the same direction as that generated by cyclic tension.

To explain this phenomenon, consider a perfectly incompressible material with $\nu = 0.5$, also poled to have a piezoelectric strain coefficient d_{33}. This results in the non-zero piezoelectric stress coefficients $e_{31} = e_{32} = \lambda d_{33}$ and $e_{33} = (\lambda + 2\mu)d_{33}$, where λ and μ are the Lamé constants. Note that, in full notation, the piezoelectric stress coefficient e_{ijk} is related to the piezoelectric strain coefficient d_{imn} through the relation [31]:

$$e_{ijk} = d_{imn} C_{mnjk} \tag{3.16}$$

where C_{mnjk} is the elasticity stiffness tensor.

From this, we can deduce $e_{31}/e_{33} = \nu/(1-\nu)$, and when $\nu = 0.5$, $e_{31} = e_{32} = e_{33}$. That is, the piezoelectric contribution from a unit principal strain in the loading direction and that from a unit principal strain in the transverse direction are equal in an incompressible material.

In the case of pure tension or compression, the Green-Lagrange strain tensor has the non-zero components $E_{11} = E_{22} = (1/\alpha - 1)/2$ and $E_{33} = (\alpha^2 - 1)/2$, where $\alpha = \alpha_3$ is the principal stretch along the loading direction. It can be seen

that $E_{11} + E_{22} + E_{33} \geq 0$ always holds, with $E_{11} + E_{22} + E_{33} = 0$ satisfied only at $\alpha = 1$, i.e. no deformation. For a perfectly incompressible material, we thus expect the generated electric field to be always in the same direction when the material is subjected to uniaxial tension and compression. In the nearly incompressible case studied, since Poissons ratio is slightly below 0.5, the piezoelectric coefficient e_{33} is slightly larger than e_{31} and e_{32}. As a result, when the material is subjected to a small amount of uniaxial compression, the contribution of E_{33} to the electric field is still stronger than the total contribution by E_{11} and E_{33}, as observed in Figure 3.3b. When the material is further deformed, the generated electric field switches direction, as seen in Figures 3.3c and 3.3d. This suggests that, by adjusting the compressibility of the p-NC material, we can control the possible direction of the piezoelectric field generated under large deformation.

To further verify the robustness of the calibrated FE model, a set of dynamic loading tests of flexible 3D piezo-shells was also simulated, with the configuration shown in Figure 3.4a. It is worthwhile to note that, in this configuration, the piezoelectric material is poled along the radial direction of the curved shell structure, and the plate is grounded across its inner surface, i.e. $\phi(r = r_i) = 0$ with r_i being the inner radius of the half-cylinder shell structure. Since the piezoelectric coupling is performed in the reference configuration, update of the piezoelectric constant tensor is not necessary during the simulation of finite deformation process. Due to the deformation field in the bent structure, the electric potential field is non-uniform along the outer surface

of the shell, with an example of typical distribution shown in Figure 3.4a. In this case, we compare the peak total surface charge Q_p across the shell surface by evaluating

$$Q_p(P_p, \omega) = \frac{\varepsilon_r \varepsilon_0}{d} \int_{A_S} \Delta\phi_P(P_p, \omega, \mathbf{x}) dA \tag{3.17}$$

where P_p is the peak compressive load applied, $\mathbf{x}$ is coordinate of the point studied on the shell surface, $\Delta\phi_p$ is the peak difference of electric potential measured across the shell thickness, and A_S is the surface of the shell structure. Once again, the simulation results are compared with the experimental measurements, as displayed in Figure 3.4b. The results are generally in good agreement, though the numerical prediction is slightly higher overall than the experimental measurement. This may be attributed to some uncertainties in the fabrication process of the piezo-shell specimens and possible charge leaking during measuring process.

3.5 Sensitivity study for optimal mechanical parameters

To provide additional guidance to the design of p-NCs, a sensitivity study was conducted with the FE model to help seek an optimal set of mechanical parameters for high piezoelectric performance. We investigate individually the effect of the three input mechanical parameters, viz. instantaneous modulus E_0, viscous relaxation μ_0, and relaxation time τ, on the peak charge output in a cyclically loaded p-NC plate

polarized in the loading direction, i.e. the configuration shown in Figure 3.2a. For a given set of (E_0, μ_0, τ), we may determine the storage modulus at an assigned loading frequency according to Equation 3.13. Then, we utilize the available data of experimentally measured pairs of storage and loss moduli in the manufactured p-NC specimens to interpolate the corresponding loss modulus $E^{''}$ given a storage modulus $E^{'}$. Experiments results, as discussed earlier, confirm that permittivity is not significantly altered by the adjustment of the mechanical parameters in the polymeric matrix. Maintaining a constant value of piezo-particle volume ratio in the composite while adjusting the parameters (E_0, μ_0, τ), the piezoelectric constant $d_{33}(E^{'}, E^{''})$ can be calculated according to Equation 3.11. In the sensitivity study, the loading condition is set to be uniaxial cyclic compression at 10Hz, with pattern described by Equation 3.11 and maximum load set to 400 Pa.

Figure 3.5 shows the change in time history of surface charge density when we adjust E_0, μ_0, and τ, respectively, while keeping the other mechanical input parameters constant between the examined sets. As indicated in Figure 3.5a, when the overall stiffness of the p-NC material is decreased, an increase in piezoelectric output is observed, which is in agreement with the experimental observations discussed earlier. In specific, a decrease of elastic modulus by 50% and 75% allowed for an increase of steady-state piezoelectric output by 36% and 76%, respectively.

In the load-control setting examined here, this is due to the overall increase of piezoelectric constant $d_{33}(E^{'}, E^{''})$ when $E^{'}$ decreases significantly. To examine this

phenomenon, we may write Equation 3.11 in a rearranged form

$$d_{33} = \varepsilon_c \sqrt{\frac{2V_{piezo}}{V\varepsilon_{piezo}}} \sqrt{\frac{E'/2 - \pi E''/4}{E'^2 + E''^2}} = \varepsilon_c \sqrt{\frac{2V_{piezo}}{V\varepsilon_{piezo}}} A(E', E'') \tag{3.18}$$

where the change of the parameter $A(E', E'')$ following the adjustment of E' and E'' dictates the change of piezoelectric performance. For the experimentally measured pairs of (E', E''), the corresponding values of $A(E', E'')$ is shown in Figure 3.5b, with $A(E', E'')$ clearly displaying a decrease when E' is greatly increased. This sheds light on why higher piezoelectric output is observed in the softer p-NC specimens, and that a lower overall modulus is desired in this class of material.

The effect of material relaxation on the piezoelectric output can be examined according to the results shown in Figure 3.5c. When one-way cyclic loading is applied to the viscoelastic material, as done in the present set of simulations, relaxation in elastic modulus leads to residual stress when the material is fully unloaded at the end of a loading cycle, which is converted to residual surface charge in the viscoelastic-piezoelectric system studied. The buildup of residual charge after each loading cycle leads to the gradual increase of peak surface charge, until the system finally reaches an equilibrium state. It can be observed from Figure 3.5c that a higher μ_0 allows for a more significant amount of relaxation in the material, and therefore a greater increase of peak surface charge after multiple cycles of one-way loading. This suggests that, for applications where one-way dynamic loading is anticipated, increased amount of

viscous relaxation is beneficial for higher piezoelectric peak output.

Figure 3.5e shows the effect of relaxation time, τ, on the time history of surface charge density. In this case, given an applied loading frequency of 10 Hz and constant E_0 and μ_0 in the material model, a moderate relaxation time, $\tau = 0.1$ s, produces higher steady-state peak surface charge than measured in the models with much shorter, $\tau = 0.01$ s, or much longer relaxation time, $\tau = 1.0$ s. This can be explained by the fact that viscoelastic solids respond to loadings in an elastic manner, when undergoing very fast or very slow processes [64–66]. When the loading cycle is very long relative to the length of the relaxation time, the viscoelastic material behaves effectively as a softened elastic solid, and minimal residual stress is accumulated during the loading-unloading process. When the loading cycle is very short relative to the relaxation time, there is insufficient time for a considerable amount of viscous energy dissipation to take place, and therefore the viscoelastic material behaves effectively as a stiff elastic solid. We may thus conclude that, when the ratio of loading cycle length to relaxation time is too low or too high, mechanical behavior of the material converges towards elasticity, and, consequentially, we are unable to take advantage of viscous relaxation to increase steady-state charge output. In order to maximize piezoelectric output, the relaxation time of the material should be tailored to match closely with the expected loading frequency. However, if it is more desirable for the effect of viscous relaxation to be minimized, the relaxation time should be adjusted to be much higher or much lower than the expected loading frequency.

3.6 Conclusion

Using the multiphysics finite element framework reviewed in Chapter 2, simulations were performed to investigate the behavior of viscoelastic p-NC systems. Numerical models were calibrated by incorporating experimentally measured mechanical properties and analytical prediction of piezoelectric constant into a multi-physics finite element framework. Sensitivity studies were performed using numerical model to investigate the relations between input parameters of the p-NC model and the piezoelectric output to provide guidance for a desired set of mechanical properties in the studied configuration.

It is found that, given cyclic compression loading with a constant value of peak load, higher loading frequency corresponds to a lower level of peak output at steady-state. Additionally, a decrease of elastic modulus allowed for an increase of steady-state piezoelectric output in the p-NC material. The effect of viscous energy dissipation can also be reduced by tailoring the material relaxation time to be much shorter or longer than the length of applied loading cycle. Based on these findings, the energy harvesting and the sensing performance of p-NCs can be further enhanced by properly harnessing the viscoelasticity of piezocomposites.

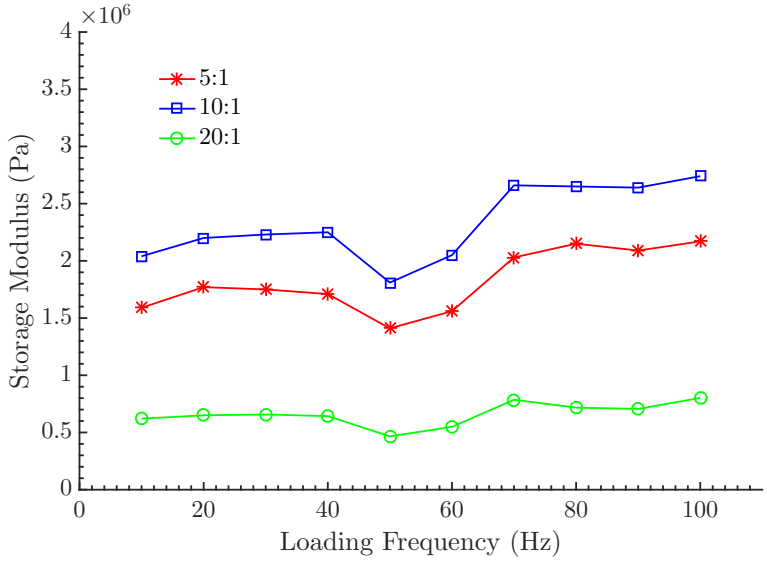

(a)

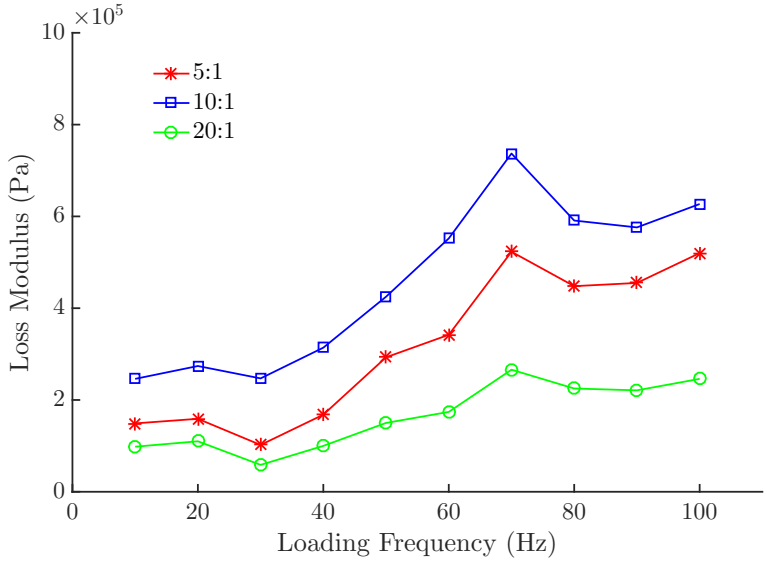

(b)

Figure 3.1: Experimental measurement of dynamic moduli in the viscoelastic p-NC specimens: (a) comparison of storage moduli at different loading frequencies; (b) comparison of loss moduli at different loading frequencies.

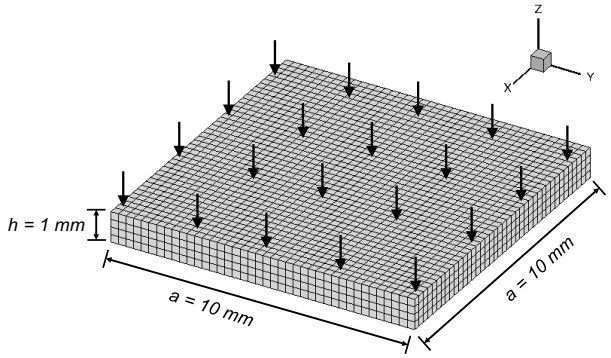

(a)

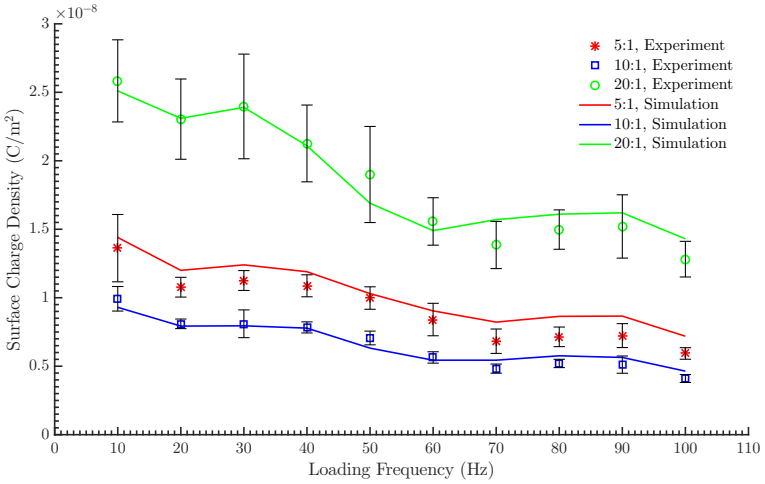

(b)

Figure 3.2: Simulation results compared with experimental results for cyclic compression of p-NC plate. (a) 3D model and mesh of the flat plate subjected to cyclic compressive loading; (b) Comparison between experimental measurements and simulation results for peak surface charge density at steady-state of loading with different frequencies, on top surface of flat plate.

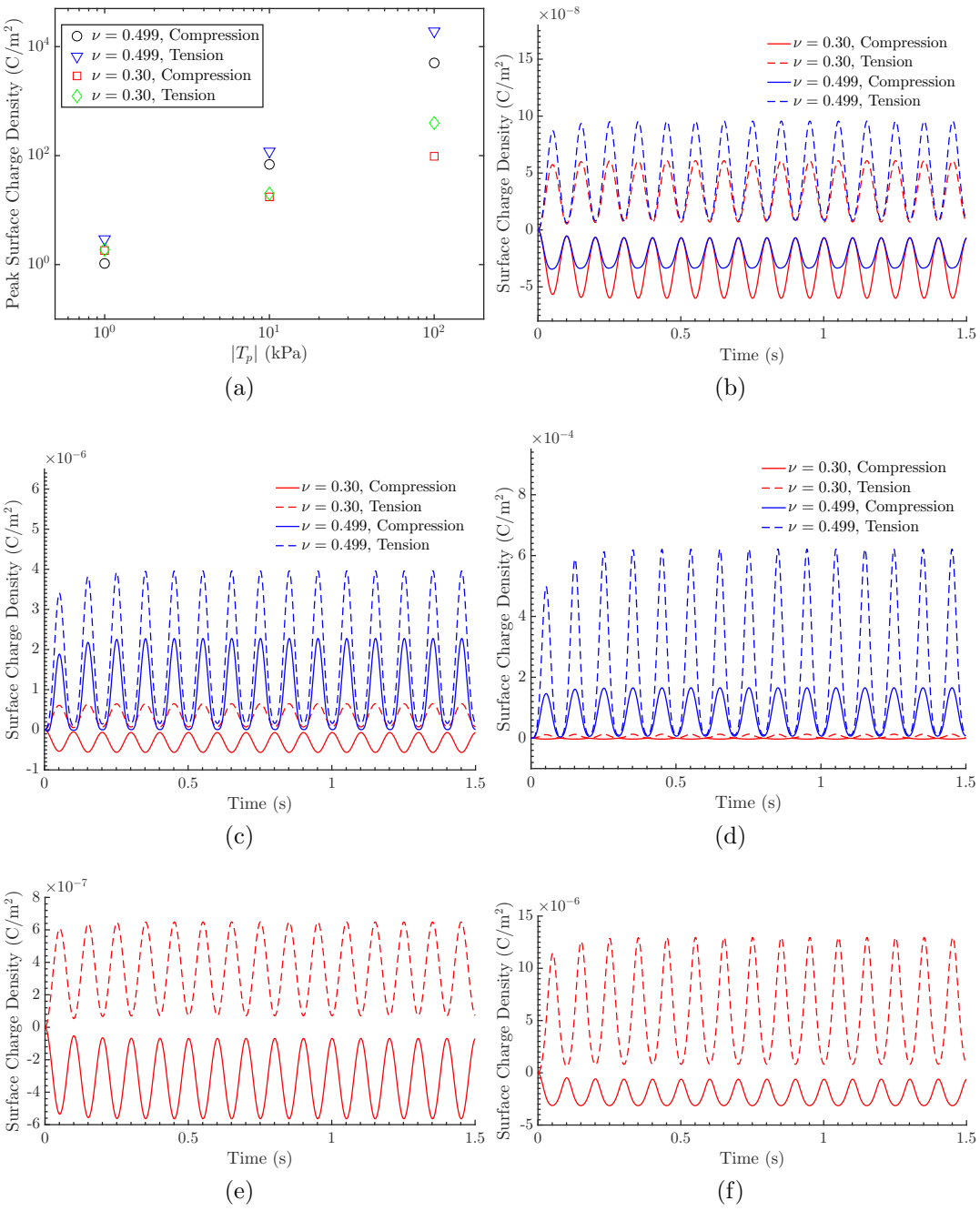

Figure 3.3: Simulation results for p-NC models under cyclic large deformation: (a) peak magnitude of surface charge density for compressible and nearly-incompressible models of 20:1 p-NC under large cyclic deformation of 10 Hz; (b),(c),(d) comparison of surface charge density time history under compressive and tensile cyclic loading of peak load magnitude 1 kPa, 10 kPa, 100 kPa; (e),(f) Detailed view of surface charge density time history under compressive cyclic loading of peak load magnitude 10 kPa, 100 kPa;

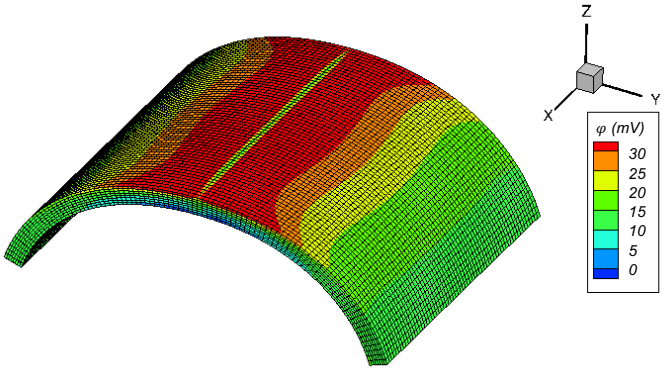

(a)

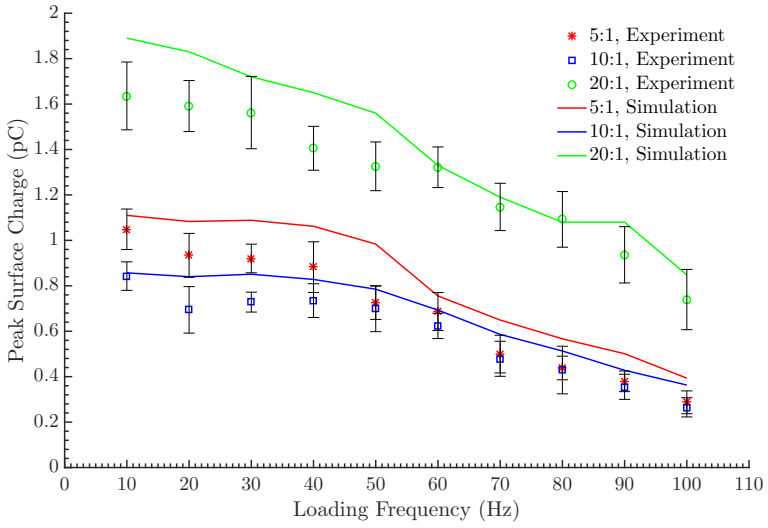

(b)

Figure 3.4: Simulation results compared with experimental results for cyclic compression of curved p-NC shell. (a) Electric potential distribution in the 3D model of a p-NC shell structure subjected to cyclic compression, poled along radial direction and grounded across inner surface; (b) Comparison between experimental measurements and simulation results for peak surface charge density at steady-state of loading with different frequencies, on top surface of flat plate.

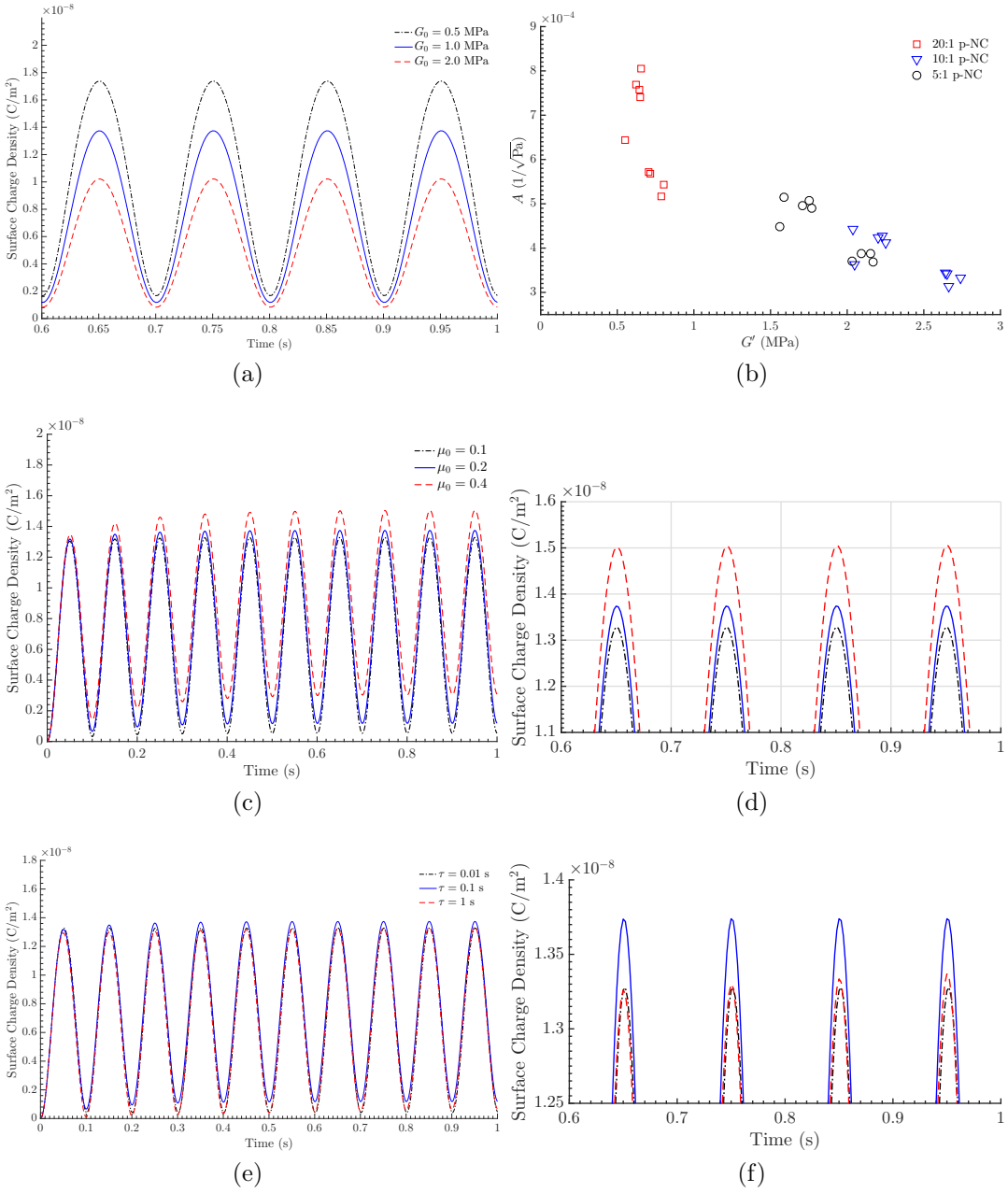

Figure 3.5: Results of sensitivity studies: (a) Time history of surface charge density, for p-NC models with different instantaneous elastic modulus E_0; (b) Dependence of viscoelastic contribution factor $A(E^{'})$ on storage modulus $E^{'}$, based on experiment measurements. (c) Time history of surface charge density, for p-NC models with different viscous relaxation proportion μ_0; (d) Detailed comparison of steady-state surface charge density, for p-NC models with different viscous relaxation proportion μ_0; (e) Time history of surface charge density, for p-NC models with different relaxation time τ; (f) Detailed comparison of steady-state surface charge density, for p-NC models with different relaxation time τ .

Chapter 4

Conclusions and Perspectives

Utilizing a multiphysics finite element model coupling transient electromagnetic and dynamic mechanical fields in the time domain, computational analysis is performed to analyze the piezoelectric behavior of viscoelastic p-NC structures under dynamic loading conditions. The process served as validation for the model framework to robustly predict the behavior of viscoelastic-piezoelectric systems subject to dynamic finite deformation. Additionally, the problems of interest in the present study are examples of coupled multiphysics problems that can be efficiently solved with the introduced computational framework.

In the model framework, the coupling scheme maps Maxwell's equations from spatial to material coordinates in the reference configuration, allowing for the analysis of finite deformation and its effect on the electromagnetic field variables. The framework is able to predict the evolution of electrical and magnetic fields in a vibrating media undergoing finite deformation, with capabilities unavailable in current commercial codes for multiphysics analysis.

Input parameters of the computational model is calibrated according to exper-

imental measurements to reproduce the piezoelectric behavior of viscoelastic p-NC structures under cyclic loading of various frequencies. Additional simulations are performed to investigate the response of the p-NC model under dynamic large deformation, further validating the capability of the finite element model to predict the piezoelectric performance of the p-NC systems.

A sensitivity study is conducted to provide additional guidance to the design of p-NCs. By adjusting the input mechanical parameters in the material model, viz. instantaneous modulus E_0, viscous relaxation μ_0, and relaxation time τ, an optimal set of mechanical parameters is determined for high piezoelectric performance. It is found that, under a load-controlled cyclic loading condition, piezoelectric output is higher in p-NC with lower instantaneous modulus. The increase of viscous relaxation, i.e. higher μ_0, corresponds to a large amount of residual stress at the end of a single-direction loading cycle. In the case of cyclic compression or cyclic tension loading, p-NC with high μ_0 produced higher peak charge output at steady-state. The effect of viscous relaxation is strongest when the relaxation time τ of the viscous material model has a magnitude comparable to the cycle length of the applied loading. When the loading cycle is much longer or shorter than the relaxation time, the p-NC behaves similar to an elastic material. According to the specific application of the material, the mechanical parameters can be tailored to produce optimal piezoelectric performance under dynamic loading conditions. The calibrated material model can be also further applied to guide the design of p-NC systems with complex structures, under different

dynamic loading conditions which cannot be easily tested with experiments. In future works, the computational model may be further improved by explicitly modeling the nanostructure of the p-NC material to accurately capture the interactions between the polymeric matrix, piezoparticles, and nanofillers.

Bibliography

[1] Xiaoliang Zhao, Huidong Gao, Guangfan Zhang, Bulent Ayhan, Fei Yan, Chiman Kwan, and Joseph L Rose. Active health monitoring of an aircraft wing with embedded piezoelectric sensor/actuator network: I. defect detection, localization and growth monitoring. *Smart materials and structures*, 16(4):1208, 2007.

[2] Jinzhu Zhou, Jin Huang, Qingqang He, Baofu Tang, and Liwei Song. Development and coupling analysis of active skin antenna. *Smart Materials and Structures*, 26(2):025011, 2016.

[3] Thomas Bailey and JE Ubbard. Distributed piezoelectric-polymer active vibration control of a cantilever beam. *Journal of Guidance, Control, and Dynamics*, 8(5):605–611, 1985.

[4] Kt Chandrashekhara and AN Agarwal. Active vibration control of laminated composite plates using piezoelectric devices: a finite element approach. *Journal of Intelligent Material Systems and Structures*, 4(4):496–508, 1993.

[5] Vladimir M Shalaev. Optical negative-index metamaterials. *Nature photonics*, 1(1):41–48, 2007.

BIBLIOGRAPHY

[6] Wenshan Cai and Vladimir Shalaev. *Optical metamaterials: fundamentals and applications*. Springer Science & Business Media, 2009.

[7] Yugang Sun, Won Mook Choi, Hanqing Jiang, Yonggang Y Huang, and John A Rogers. Controlled buckling of semiconductor nanoribbons for stretchable electronics. *Nature nanotechnology*, 1(3):201–207, 2006.

[8] Alfred J Baca, Jong-Hyun Ahn, Yugang Sun, Matthew A Meitl, Etienne Menard, Hoon-Sik Kim, Won Mook Choi, Dae-Hyeong Kim, Young Huang, and John A Rogers. Semiconductor wires and ribbons for high-performance flexible electronics. *Angewandte Chemie International Edition*, 47(30):5524–5542, 2008.

[9] John A Rogers, Takao Someya, and Yonggang Huang. Materials and mechanics for stretchable electronics. *Science*, 327(5973):1603–1607, 2010.

[10] Nanshu Lu and Shixuan Yang. Mechanics for stretchable sensors. *Current Opinion in Solid State and Materials Science*, 19(3):149–159, 2015.

[11] Tayfun Ozdemir and John L Volakis. Triangular prisms for edge-based vector finite element analysis of conformal antennas. *IEEE Transactions on Antennas and Propagation*, 45(5):788–797, 1997.

[12] Waldemar Rachowicz and L Demkowicz. An hp-adaptive finite element method for electromagneticspart ii: A 3d implementation. *International journal for numerical methods in engineering*, 53(1):147–180, 2002.

BIBLIOGRAPHY

[13] Witold Cecot, Waldemar Rachowicz, and L Demkowicz. An hp-adaptive finite element method for electromagnetics. part 3: A three-dimensional infinite element for maxwell's equations. *International journal for numerical methods in engineering*, 57(7):899–921, 2003.

[14] Leszek Demkowicz, Jason Kurtz, and Frederick Qiu. hp-adaptive finite elements for coupled multiphysics wave propagation problems. *Computer Methods in Mechanics*, pages 19–42, 2010.

[15] Jesse D Thomas and Nicolas Triantafyllidis. On electromagnetic forming processes in finitely strained solids: Theory and examples. *Journal of the Mechanics and Physics of Solids*, 57(8):1391–1416, 2009.

[16] Jesse D Thomas, Nicolas Triantafyllidis, A Vivek, Glenn S Daehn, and John R Bradley. Comparison of fully coupled modeling and experiments for electromagnetic forming processes in finitely strained solids. *International Journal of Fracture*, 163(1):67–83, 2010.

[17] AS Semenov, H Kessler, A Liskowsky, and H Balke. On a vector potential formulation for 3d electromechanical finite element analysis. *International Journal for Numerical Methods in Biomedical Engineering*, 22(5):357–375, 2006.

[18] Alejandro Mota and Jonathan A Zimmerman. A variational, finite-deformation constitutive model for piezoelectric materials. *International journal for numerical methods in engineering*, 85(6):752–767, 2011.

[19] Shu Guo and Somnath Ghosh. A finite element model for coupled 3d transient electromagnetic and structural dynamics problems. *Computational Mechanics*, 54(2):407–424, 2014.

[20] Reza Yaghmaie, Shu Guo, and Somnath Ghosh. Wavelet transformation induced multi-time scaling (watmus) model for coupled transient electro-magnetic and structural dynamics finite element analysis. *Computer Methods in Applied Mechanics and Engineering*, 303:341–373, 2016.

[21] Shu Guo. *A Coupled Multi-physics Analysis Model for Integrating Transient Electro-Magnetics and Structural Dynamic Fields with Damage*. PhD thesis, Johns Hopkins University, 2017.

[22] M Lax and DF Nelson. Maxwell equations in material form. *Physical Review B*, 13(4):1777, 1976.

[23] Carmine Trimarco. Material electromagnetic fields and material forces. *Archive of Applied Mechanics*, 77(2):177–184, 2007.

[24] Carmine Trimarco. On the dynamics of electromagnetic bodies. *International Journal of Advances in Engineering Sciences and Applied Mathematics*, 1(4):157–162, 2009.

[25] Juan Carlos Simo. On a fully three-dimensional finite-strain viscoelastic damage

model: formulation and computational aspects. *Computer methods in applied mechanics and engineering*, 60(2):153–173, 1987.

[26] Olgierd Cecil Zienkiewicz and Robert Leroy Taylor. *The finite element method: solid mechanics*, volume 2. Butterworth-heinemann, 2000.

[27] Donald Frederick Nelson. *Electric, optic, and acoustic interactions in dielectrics*. John Wiley & Sons, 1979.

[28] L Vu-Quoc, V Srinivas, and Y Zhai. A generalized unit system for concise electromagnetic formulation and accurate numerical solutions. *Journal of Computational Physics*, 181(2):407–429, 2002.

[29] Jian-Ming Jin. *The finite element method in electromagnetics*. John Wiley & Sons, 2015.

[30] W Nowacki. Foundations of linear piezoelectricity. *Electromagnetic interactions in elastic solids*, 257:105–157, 1979.

[31] A Meitzler, HF Tiersten, AW Warner, D Berlincourt, GA Couqin, and FS Welsh III. Ieee standard on piezoelectricity, 1988.

[32] C Miehe, D Rosato, and B Kiefer. Variational principles in dissipative electro-magneto-mechanics: A framework for the macro-modeling of functional materials. *International Journal for Numerical Methods in Engineering*, 86(10):1225–1276, 2011.

BIBLIOGRAPHY

[33] Gerhard A Holzapfel. Nonlinear solid mechanics. 2000.

[34] João Pedro A Bastos and Nelson Sadowski. *Electromagnetic modeling by finite element methods*. CRC press, 2003.

[35] Klaus-Jürgen Bathe and Edward L Wilson. *Numerical methods in finite element analysis*, volume 197. Prentice-Hall Englewood Cliffs, NJ, 1976.

[36] K Subbaraj and MA Dokainish. A survey of direct time-integration methods in computational structural dynamicsii. implicit methods. *Computers & Structures*, 32(6):1387–1401, 1989.

[37] MA Dokainish and K Subbaraj. A survey of direct time-integration methods in computational structural dynamicsi. explicit methods. *Computers & Structures*, 32(6):1371–1386, 1989.

[38] George Karypis, Kirk Schloegel, and Vipin Kumar. Parmetis: Parallel graph partitioning and sparse matrix ordering library. *Version 1.0, Dept. of Computer Science, University of Minnesota*, 1997.

[39] Satish Balay, J Brown, Kris Buschelman, Victor Eijkhout, W Gropp, D Kaushik, M Knepley, L Curfman McInnes, B Smith, and Hong Zhang. Petsc users manual revision 3.5. *Argonne National Laboratory (ANL)*, 2014.

[40] Zhong Lin Wang and Jinhui Song. Piezoelectric nanogenerators based on zinc oxide nanowire arrays. *Science*, 312(5771):242–246, 2006.

[41] Luana Persano, Canan Dagdeviren, Yewang Su, Yihui Zhang, Salvatore Girardo, Dario Pisignano, Yonggang Huang, and John A Rogers. High performance piezoelectric devices based on aligned arrays of nanofibers of poly (vinylidenefluoride-co-trifluoroethylene). *Nature communications*, 4:1633, 2013.

[42] Geon-Tae Hwang, Hyewon Park, Jeong-Ho Lee, SeKwon Oh, Kwi-Il Park, Myunghwan Byun, Hyelim Park, Gun Ahn, Chang Kyu Jeong, Kwangsoo No, et al. Self-powered cardiac pacemaker enabled by flexible single crystalline pmn-pt piezoelectric energy harvester. *Advanced materials*, 26(28):4880–4887, 2014.

[43] Po-Kang Yang, Long Lin, Fang Yi, Xiuhan Li, Ken C Pradel, Yunlong Zi, Chih-I Wu, Hau He Jr, Yue Zhang, and Zhong Lin Wang. A flexible, stretchable and shape-adaptive approach for versatile energy conversion and self-powered biomedical monitoring. *Advanced Materials*, 27(25):3817–3824, 2015.

[44] Xu Xiao, Longyan Yuan, Junwen Zhong, Tianpeng Ding, Yu Liu, Zhixiang Cai, Yaoguang Rong, Hongwei Han, Jun Zhou, and Zhong Lin Wang. High-strain sensors based on zno nanowire/polystyrene hybridized flexible films. *Advanced materials*, 23(45):5440–5444, 2011.

[45] Santiago Orrego, Kourosh Shoele, Andre Ruas, Kyle Doran, Brett Caggiano, Rajat Mittal, and Sung Hoon Kang. Harvesting ambient wind energy with an inverted piezoelectric flag. *Applied Energy*, 194:212–222, 2017.

[46] Sangmin Lee, Sung-Hwan Bae, Long Lin, Ya Yang, Chan Park, Sang-Woo Kim,

Seung Nam Cha, Hyunjin Kim, Young Jun Park, and Zhong Lin Wang. Superflexible nanogenerator for energy harvesting from gentle wind and as an active deformation sensor. *Advanced Functional Materials*, 23(19):2445–2449, 2013.

[47] Rusen Yang, Yong Qin, Cheng Li, Guang Zhu, and Zhong Lin Wang. Converting biomechanical energy into electricity by a muscle-movement-driven nanogenerator. *Nano Letters*, 9(3):1201–1205, 2009.

[48] Guang Zhu, Rusen Yang, Sihong Wang, and Zhong Lin Wang. Flexible high-output nanogenerator based on lateral zno nanowire array. *Nano letters*, 10(8):3151–3155, 2010.

[49] Yi Qi, Noah T Jafferis, Kenneth Lyons Jr, Christine M Lee, Habib Ahmad, and Michael C McAlpine. Piezoelectric ribbons printed onto rubber for flexible energy conversion. *Nano letters*, 10(2):524–528, 2010.

[50] Yi Qi, Jihoon Kim, Thanh D Nguyen, Bozhena Lisko, Prashant K Purohit, and Michael C McAlpine. Enhanced piezoelectricity and stretchability in energy harvesting devices fabricated from buckled pzt ribbons. *Nano letters*, 11(3):1331–1336, 2011.

[51] Kwi-Il Park, Sheng Xu, Ying Liu, Geon-Tae Hwang, Suk-Joong L Kang, Zhong Lin Wang, and Keon Jae Lee. Piezoelectric batio3 thin film nanogenerator on plastic substrates. *Nano letters*, 10(12):4939–4943, 2010.

BIBLIOGRAPHY

[52] Chieh Chang, Van H Tran, Junbo Wang, Yiin-Kuen Fuh, and Liwei Lin. Direct-write piezoelectric polymeric nanogenerator with high energy conversion efficiency. *Nano letters*, 10(2):726–731, 2010.

[53] Minbaek Lee, Chih-Yen Chen, Sihong Wang, Seung Nam Cha, Yong Jun Park, Jong Min Kim, Li-Jen Chou, and Zhong Lin Wang. A hybrid piezoelectric structure for wearable nanogenerators. *Advanced Materials*, 24(13):1759–1764, 2012.

[54] Kwi-Il Park, Minbaek Lee, Ying Liu, San Moon, Geon-Tae Hwang, Guang Zhu, Ji Eun Kim, Sang Ouk Kim, Do Kyung Kim, Zhong Lin Wang, et al. Flexible nanocomposite generator made of batio3 nanoparticles and graphitic carbons. *Advanced Materials*, 24(22):2999–3004, 2012.

[55] Ke Yang, Xingyi Huang, Yanhui Huang, Liyuan Xie, and Pingkai Jiang. Fluoropolymer@ batio3 hybrid nanoparticles prepared via raft polymerization: toward ferroelectric polymer nanocomposites with high dielectric constant and low dielectric loss for energy storage application. *Chemistry of Materials*, 25(11):2327–2338, 2013.

[56] Sung-Ho Shin, Young-Hwan Kim, Min Hyung Lee, Joo-Yun Jung, and Junghyo Nah. Hemispherically aggregated batio3 nanoparticle composite thin film for high-performance flexible piezoelectric nanogenerator. *ACS nano*, 8(3):2766–2773, 2014.

BIBLIOGRAPHY

[57] Indu Babu and Gijsbertus de With. Highly flexible piezoelectric 0–3 pzt–pdms composites with high filler content. *Composites Science and Technology*, 91:91–97, 2014.

[58] HM Ning, N Hu, T Kamata, JH Qiu, X Han, LM Zhou, Christiana Chang, Y Liu, LK Wu, HL Ji, et al. Improved piezoelectric properties of poly (vinylidene fluoride) nanocomposites containing multi-walled carbon nanotubes. *Smart materials and structures*, 22(6):065011, 2013.

[59] Vahabodin Goodarzi and Mohammad Reza Saeb. Modeling and interpreting particle shape dependence of electric displacement distribution in the piezoelectric polymer composites. *Journal of Intelligent Material Systems and Structures*, 27(17):2395–2407, 2016.

[60] Shogo Mamada, Naoyuki Yaguchi, Masanori Hansaka, Masafumi Yamato, and Hirohisa Yoshida. Matrix influence on the piezoelectric properties of piezoelectric ceramic/polymer composite exhibiting particle alignment. *Journal of Applied Polymer Science*, 132(15), 2015.

[61] Nicholas W Tschoegl. *The phenomenological theory of linear viscoelastic behavior: an introduction*. Springer Science & Business Media, 2012.

[62] Norman Gerard McCrum, CP Buckley, and Clive B Bucknall. *Principles of polymer engineering*. Oxford University Press, USA, 1997.

BIBLIOGRAPHY

[63] Richard Christensen. *Theory of viscoelasticity: an introduction*. Elsevier, 2012.

[64] Roderic S Lakes. *Viscoelastic materials*. Cambridge University Press, 2009.

[65] Clarence Zener. *Elasticity and anelasticity of metals*. University of Chicago press, 1948.

[66] John D Ferry. *Viscoelastic properties of polymers*. John Wiley & Sons, 1980.

Vita

Zhiren Zhu was born in Sendai, and spent childhood years living in Japan, the United States, Norway, and China. Zhiren received the B.S. degree in Civil Engineering from the University of Massachusetts Amherst in 2013 and the M.S. degree in Structural Engineering and Mechanics from the University of Minnesota, Minneapolis in 2015.

Starting in August 2017, Zhiren will work as a junior foundations engineer at Berkel and Company Contractors in Silver Spring, MD.